metals

*Article*

# A Method to Optimize Parameters Development in L-PBF Based on Single and Multitracks Analysis: A Case Study on Inconel 718 Alloy

**Alessandro Giorgetti [1,2,*], Niccolò Baldi [2,3], Marco Palladino [3], Filippo Ceccanti [3], Gabriele Arcidiacono [2] and Paolo Citti [2]**

[1] Department of Industrial, Electronic and Mechanical Engineering, Roma Tre University, 00146 Rome, Italy
[2] Department of Engineering Science, Guglielmo Marconi University, 00193 Rome, Italy
[3] Baker Hughes—Nuovo Pignone, Via Felice Matteucci 2, 50127 Florence, Italy
* Correspondence: alessandro.giorgetti@uniroma3.it

**Abstract:** In the context of the use of AM, particularly in the L-PBF technique, the printability characterization of material occurs through the identification of its printability map as a function of printing process parameters. The printability map identifies the region where the powder melting is optimal and ensures a dense and defect-free material. Identifying the zones affected by physical phenomena that occur during the printing process which lead to material defects such as keyhole, lack of fusion and balling mode is also possible. Classical methods for the characterization of material and the identification of its printability map require the printing of a large number of specimens. The analysis of the specimens is currently time-consuming and costly. This paper proposed a methodology to identify optimal process parameters in L-PBF using an integrated single and multi-tracks analyses embedded in an overall algorithm with detailed metrics and specific factors. The main scope is to speed up the identification of printability window and, consequently, material characterization, reducing the number of micrographic analyses. The method is validated through an experimental campaign assessing the material microstructure in terms of porosity and melt pool evaluation. The case study on IN718 superalloy shows how the application of the proposed method allows an important reduction of micrographic analysis. The results obtained in the case study are a reduction of 25% for the complete definition of the printability map and more than 90% for identifying the zone with a high productivity rate.

**Keywords:** laser powder bed fusion; single track; multi-tracks; melt pool morphology; nickel-based superalloy; Inconel 718; printability map; process parameters optimization

check for updates

**Citation:** Giorgetti, A.; Baldi, N.; Palladino, M.; Ceccanti, F.; Arcidiacono, G.; Citti, P. A Method to Optimize Parameters Development in L-PBF Based on Single and Multitracks Analysis: A Case Study on Inconel 718 Alloy. *Metals* **2023**, *13*, 306. https://doi.org/10.3390/met13020306

Academic Editor: Pavel Krakhmalev

Received: 27 December 2022
Revised: 27 January 2023
Accepted: 31 January 2023
Published: 2 February 2023

## 1. Introduction

Additive Manufacturing (AM) facilitates structure and component fabrication in a layer-by-layer deposition [1–7] and is revolutionizing the manufacturing industry due to its ability to obtain near-net-shape parts with almost no material waste [8–10]. Moreover, compared to conventional manufacturing processes, AM techniques do not use expensive tooling or dies, significantly reducing the lead time for the manufactured parts [11,12].

Laser Powder Bed Fusion (L-PBF) is the evolution of Direct Metal Laser Sintering, introduced by EOS in 1994, and is probably the most widely used and versatile AM technique, considered the most promising [13]. Compared to the other AM processes, several advantages can be pointed out [14–16], in particular:

- lower heat in L-PBF induces lower distortions, which allows a higher dimensional precision for the final part [11];
- L-PBF technique is suitable for many materials, especially for engineering metal alloys;
- L-PBF can be conducted at a much higher speed with lower material cost.

The technological advancements in metal printing over the last years have led to the rapid proliferation of L-PBF AM across various industrial sectors such as aviation, energy, oil, gas and medical. This has led to significant investments in developing industrial applications where the printed parts were increasingly larger and more complex and had to meet more stringent quality and functional requirements. The ability to significantly reduce weight while maintaining the mechanical and performance requirements of the component made L-PBF widely used in the aerospace industry [11,17]. Furthermore, the possibility of producing very complex lattice structures and customizing implants to each patient-specific anatomy was vital in developing and implementing L-PBF parts in the biomedical industry [11]. The production of gas turbine components such as fuel burners, blades and nozzles manufactured in L-PBF is becoming increasingly common in the oil and gas industry, allowing the printability of metal superalloys resistant to high temperatures that are difficult to machine and manufacture with subtractive technique.

With these advantages, the rapid manufacturing of geometrically complex near-net-shape parts can be achieved by the L-PBF process with acceptable surface integrity that can be improved through post-processing operation [18,19]. This aspect is of great importance for nickel-based superalloys, such as Inconel 718, because the low thermal conductivity and high hardness make these alloys quite difficult to manufacture using conventional machining methods [1,20,21].

During the characterization phase of the material in L-PBF, in order to avoid the presence of defects such as porosity [22] or cracks [23–26], which could severely affect the microstructure and mechanical properties of the material, many aspects of the printing process have to be studied [19]. Among these, the identification of the printability window [27,28] (Figure 1) is necessary and fundamental to have a material that is fully dense and free of processing-related defects [19]. The presence of these defects generates a modification in the mechanical properties of the materials [29]. The defect-free printability zone is identified by selecting the proper set of process parameters to ensure a proper melting of the powder bed.

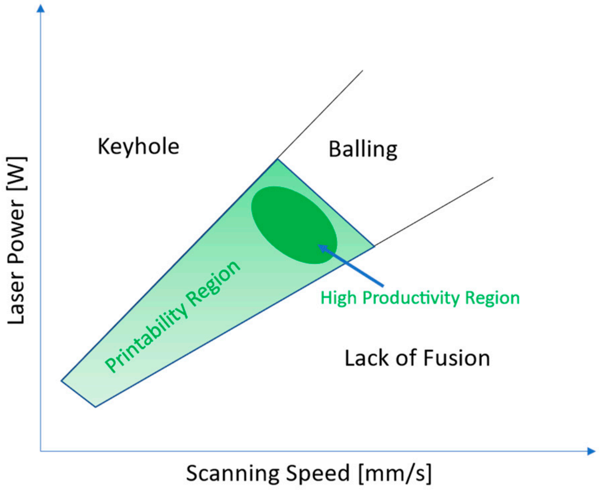

**Figure 1.** Printability map with the identification of the different zones.

Among the numerous process parameters [30–33] that directly or indirectly affect the L-PBF process, the most influential are laser power, scanning speed, hatch distance and layer thickness. In particular, it is also known that laser power and scanning speed control the geometry and melt pool formation (according to [10,20,31–34]).

The individuation of correct values of these parameters allows the melting of the powder in a conductive mode [35,36] and avoids phenomena such as keyhole [37–39], lack of fusion and balling [32,37,40–42].

Identifying the printability window for material during the L-PBF process usually requires printing many specimens and their subsequent analysis to evaluate the material density and the possible presence of defects.

The analysis of specimens needs the realization of materials sections parallel to the printing direction that need resin embedding and polishing to evaluate the material's microstructure; in particular, porosity and melt pool analyses are performed to calculate the density and the melting regime for the investigated configuration.

The preparation (cutting, etching and polishing) of a large number of specimens to perform the necessary micrographic analysis with an Optical Microscope (OM) and Scanning Electron Microscope (SEM) is costly and time-consuming.

The L-PBF process is continuously evolving to be more and more competitive in terms of productivity [43] compared to the classic technologies of subtractive manufacturing. This evolution is mainly related to the following aspects:

- The frequent modification/upgrade of machines for firmware updates, the introduction of new models with different recoating systems, gas flow distribution, base plate dimensions, number of heat sources (e.g., single-laser/multi-laser);
- The development of highly productive process parameters with high values of scanning speed, hatch distance and layer thickness [10,27,42];
- The introduction of new materials with a higher productivity rate (through the increment of scanning speed).

For all these reasons, a re-characterization of the material is frequently needed.

Therefore, developing methods that reduce the cost and the time to define a reliable printability map has become progressively more critical.

The printing of single and multi-tracks [44–52] has proven to be a very effective tool for optimizing and developing process parameters such as laser power, scanning speed and hatch distance.

In particular, with single track printing, i.e., a single laser exposure, the laser power and scanning speed values are optimized to have a sufficiently stable melt pool in terms of depth and width to ensure proper remelting of the previous layer. Multi-track printing, on the other hand, is aimed at optimizing the distance between hatch vectors, hatch distance, to ensure a sufficient overlap zone between adjacent tracks and to avoid unmelted powder within the consolidated material.

Although single and multi-track printing, the latter to a lesser extent, have been used to study various phenomena in the L-PBF process as an effect of preheating temperature [53] or interlayers cooling time [54] on melt pool shape and material density. However, these studies lack metrics and factors to enable the proper use of these tools to speed up the development of process parameters and the identification of the printability window for a material. Moreover, it is the authors' opinion that all the approaches proposed in the literature do not provide sufficient structured guidelines that can drive the optimization process, particularly considering the multi-track analysis [55,56].

This paper aims to introduce a methodology to identify optimal process parameters in L-PBF using integrated single and multi-tracks analyses embedded in an overall algorithm with detailed metrics and specific factors. The first scope of the approach is to reduce the number of micrographic analyses and consequently speed up the identification of the printability window, maintaining, at the same time, sufficient information on the microstructure and melting regime of the material. Secondly, the use of the method can drive through the various steps to identify the best process parameter set.

The structure of the paper is organized as follows: in Section 2, the proposed method is described in detail. Section 3 shows the results obtained using the proposed method and the standard approach with massive microstructure analysis for a case study on Inconel 718 alloy. Section 4 discusses the value obtained in the case study with the proposed method in evaluating a reliable printability map or identifying the most productive configuration of the power, scanning speed and hatch distance. Finally, Section 5 presents the conclusion and proposes developments for further investigations.

## 2. Materials and Methods

The method proposed in this paper consists of two main steps: the screening phase and the optimization phase. The whole approach introduced is summarized in Figure 2 and the various steps and sub-steps are described in the following paragraphs.

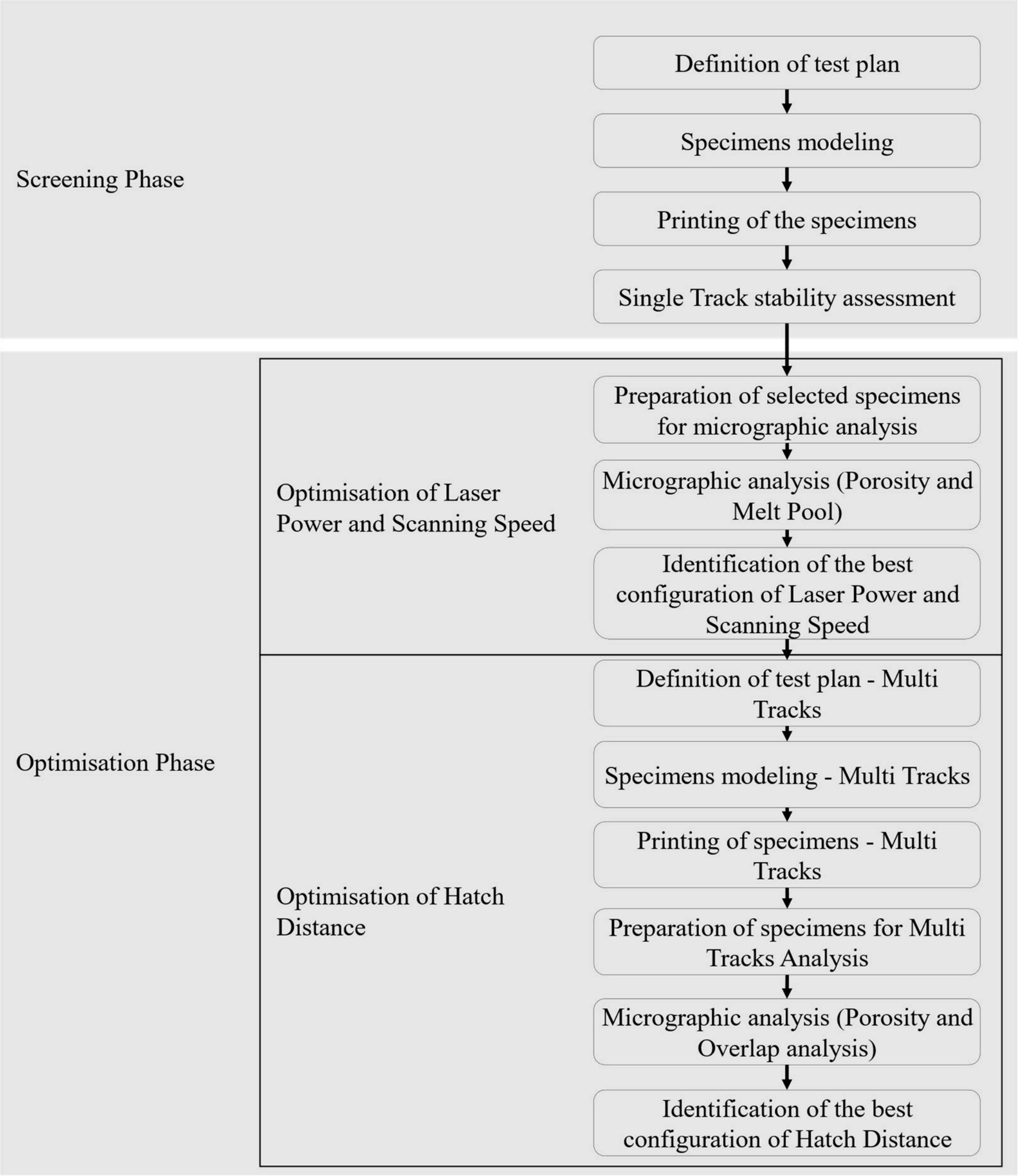

**Figure 2.** Flowchart of the method.

### *2.1. Screening Phase*

The screening phase consists of four steps:

- Definition of the test plan for the screening phase
- Specimens modelling for the screening phase
- Printing of the specimens for the screening phase
- Single track stability assessment

The single-track method, developed in many studies [45–49], is chosen to carry out the screening phase. This phase aims to reduce the number of configurations subjected to micrographic analysis using a screening approach among the configurations of the test plan obtained with a Design of Experiments (DOE).

### 2.1.1. Definition of the Test Plan for the Screening Phase

A 2D grid of experimental points is created using a DOE approach to study laser power and scanning speed effects. In particular, the range of the parameters can be chosen using results present in the literature or obtained by commercial simulation tools. This also applies to the selection of hatch distance range which is kept fixed in this phase. The number of grid points depends on the number of levels to investigate the scanning speed and laser power. So, depending on the level of accuracy required in the study, the grid may have different levels investigated.

### 2.1.2. Specimen Modelling for the Screening Phase

The specimens analyzed in this paper are modelled with the following specification (Figure 3a). The specimens are modelled as cubes of size 10 × 10 × 10 mm (body) suitable to obtain representative cross-sections and ten single tracks are made on top of them to evaluate the process's stability.

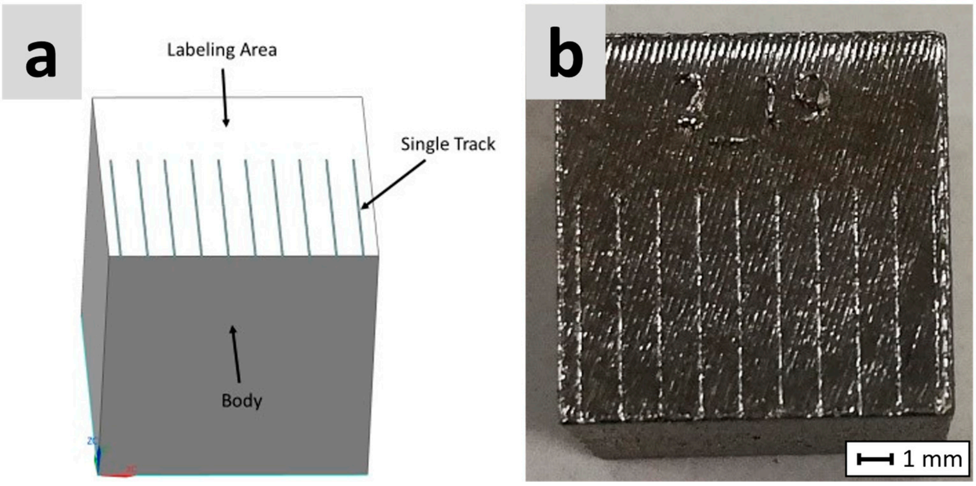

**Figure 3.** Specimen design: (**a**) CAD model, (**b**) example of the printed specimen.

The tracks' width is chosen to expose this part of the model as a single and continuous hatch. The spacing between the tracks is determined to avoid an overlap of the melt pool. As for the length of the tracks, it must be enough to label the top of the specimens; in our case, it is 6 mm.

### 2.1.3. Printing of the Specimens for the Screening Phase

The specimen modelled is exported using STL format from CAD software. The Body of the specimen and the single tracks are exported separately to print the single track on a smooth surface. The specimens are labelled, as shown in Figure 3b, to ensure the traceability of the test. Then the build file with material license and process parameters is created. After the printing, the specimens are removed from the base plate using wire-cutting technology. Once removed, the specimens are finally immersed in an acetone solution, subjected to ultrasonic cleaning to remove any powder (that could influence the results) and finally dried.

### 2.1.4. Single Track Stability Assessment

The stability of a single track is evaluated using a SEM image; each acquisition is carried out with a 40× magnification. Then, a track stability map is created using the SEM-acquired images.

This phase is a screening phase because the evaluation of the stability level of the tracks is used to select which specimens need micrographic analysis.

The stability of the tracks [50] is quantified and evaluated using the following approach (Figure 4):

(1) Check for interruptions along the tracks (in this paper it is considered interruptions the non-melting of powder for at least ten microns of length); all the tracks with an interruption must be considered unstable (Figure 5)
(2) For the tracks with no interruptions, evaluate and quantify the presence of section changes (*S*) according to the following steps:
    (A) Divide the track into five fields and, for each one, measure the width, avoiding taking into account the beginning of the track being areas where the melt pool is not yet stable (Figure 6);
    (B) Calculate the average width for each track;
    (C) Evaluate the presence of section change along the tracks; a change of section has to be considered if the measured value of the tracks' width is not comprised in tolerance of plus or minus 30% from the average track width;
    (D) Repeat from point (A) for five random tracks for each specimen.
(3) Depending on the number of sections changes, the tracks are considered:
    (A) Not stable if $S > k1$;
    (B) Metastable if $k1 < S < k2$;
    (C) Stable $S < k2$.

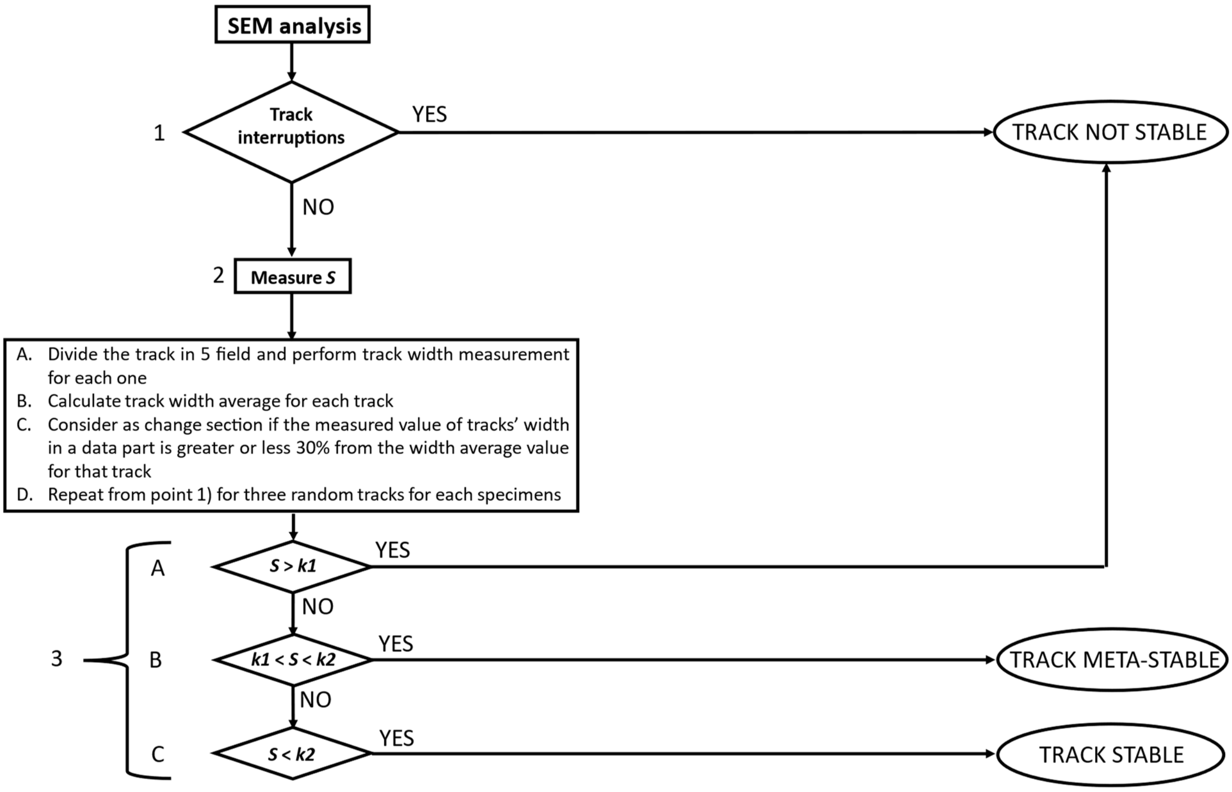

**Figure 4.** Flowchart of track stability evaluation method.

The presented screening phase can reduce the risk of performing micrographic analysis on specimens that might present a lack of fusion or balling. The presence of interruptions or a large number of section changes along the track indicates a strong instability of the melting regime and a poor melting of the underlying powder bed which can be a symptom of balling [38] and lack of fusion phenomena. Therefore, single-track stability assessment effectively identifies the sample's melting regime without resorting to expensive and time-consuming micrographic analysis.

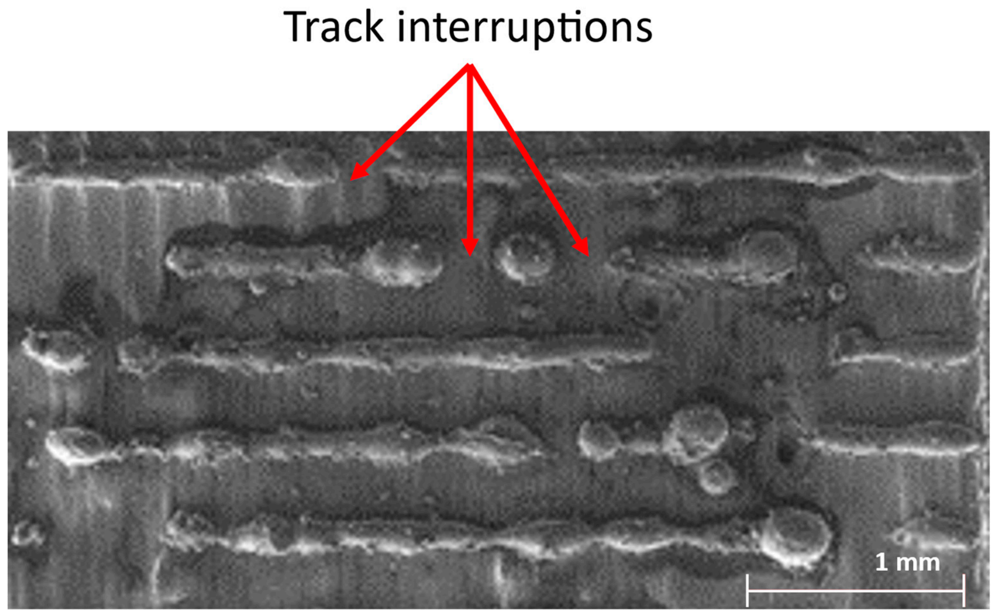

**Figure 5.** Example of track interruptions.

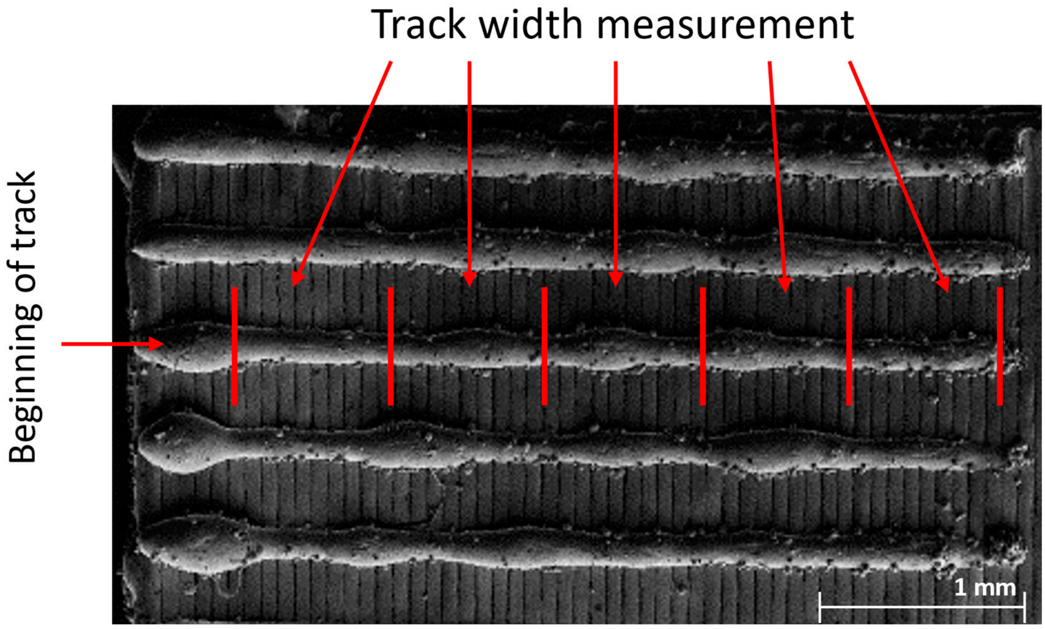

**Figure 6.** Track average measurement.

## *2.2. Optimization Phase*

The optimization phase is divided into two sub-phases that are performed in the following sequence:

1. Optimization of laser power and scanning speed (at a fixed value of hatch distance) is performed by analyzing the melt pool shape of a cross-section of single tracks. This sub-phase consists of the following steps:
    - Preparation of selected specimens for micrographic analysis
    - Micrographic analysis (porosity and melt pool)
    - Identification of the best configuration for laser power and scanning speed.
2. Optimization of hatch distance on the best configuration using multi tracks analysis. This sub-phase consists of the following steps:
    - Definition of the test plan for multi tracks analysis

- Specimens modelling for multi tracks analysis
- Printing of specimens for multi tracks analysis
- Preparation of specimens for micrographic analysis
- Micrographic analysis (porosity and overlap analysis)
- Identification of the best configuration of hatch distance.

### 2.2.1. Optimization of Laser Power and Scanning Speed

The samples selected as best in terms of track stability from the previous analysis are cut along a cross-section in the z-direction, embedded in conductive resin and properly polished to be suitable for micrographic analysis.

The microstructural analysis is performed on the prepared specimens using an optical microscope, a. The analysis comprises two phases: a porosity analysis and a melt-pool analysis. The porosity analysis is performed using appropriate sections of the specimens (e.g., Figure 7) and image analysis software (such as ImageJ or Leica software) to calculate the per cent porosity to assess the density of specimens.

In order to evaluate the melt pool shape, the specimens are etched using oxalic acid or a similar acid. The specimens are then analyzed using an optical microscope. For the assessment of the melting regime of powder, the depth and the width of the melt pool are measured; see Figure 8a,b. Using these dimensions to calculate specific parameters makes it possible to identify the heat transfer regime for each specimen [38]. The shape of at least five random single tracks is analyzed to evaluate process variability.

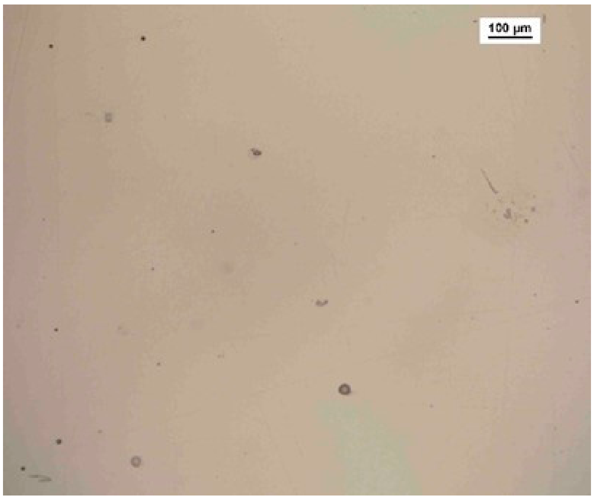

**Figure 7.** Sample's microstructure at 100× magnification.

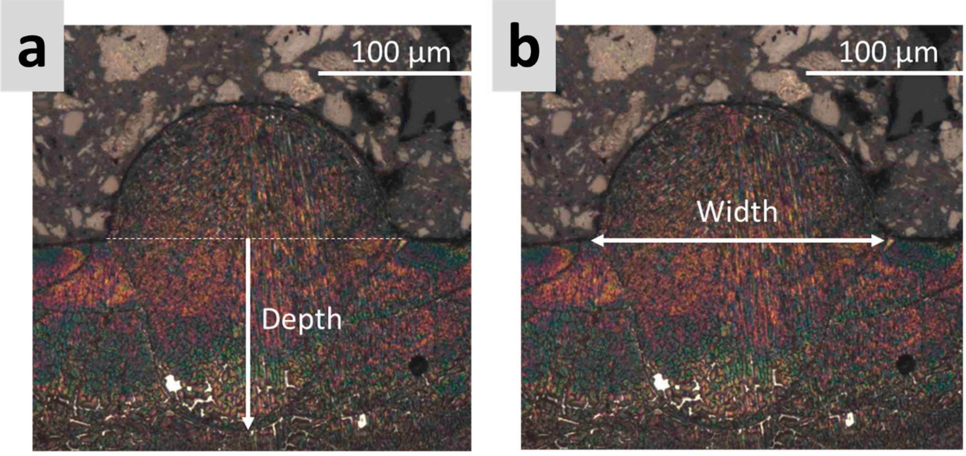

**Figure 8.** Melt pool's measurement: (**a**) depth; (**b**) width.

The expected outcome of this analysis is to select among the specimens analyzed the one that presents a conductive regime; if more than one configuration satisfies this condition, choose the specimen that is most appropriate for the activity under consideration (e.g., maximum of productivity). This step's results permit identifying the specimen with the best laser power and scanning speed value.

### 2.2.2. Optimization of Hatch Distance on the Best Configuration Using Multi-Tracks Analysis

The best configuration obtained from the previous phase is investigated at different hatch distances using three to six levels [51,52].

A specific model is realized to investigate different levels of hatch distance, as shown in Figure 9. A thick plate characterizes the model split into many sub-parts equal to the number of hatch levels; in Figure 9, three levels of hatch distances (I, II and III) are investigated. A set of multi-tracks and single tracks (equal or greater than five) are printed on the top surface of each sub-part using the procedure described in Section 2.1.2.

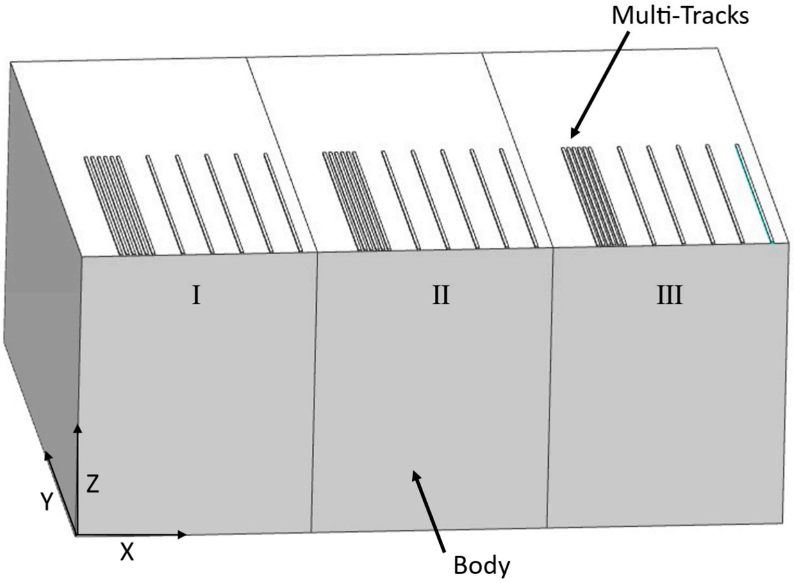

**Figure 9.** Specimens for multi-tracks analysis.

The same procedure used for single tracks (described in Section 2.2.1) is used to measure the porosity percent and prepare the specimens also in the case of multi-tracks analysis.

The purpose of multi-tracks analysis, as described in [37], is to evaluate the interaction between adjacent tracks to evaluate and replicate the printing condition on the final component (composed of several adjacent tracks on each layer).

In order to assess if the investigated hatch distance value ensures a correct overlap zone in terms of depth and width, the following method is used (Figures 10 and 11):

1- Perform a width (*W*) measurement for the three tracks within the considered multi-tracks set and calculate the average width;
2- Measure the overlap width (*OW*). The *OW* is defined as the part of the *W* dimension common among two adjacent tracks. This distance has to be greater or equal to "*k*3" times the track width (*W*) measured in step 1 to avoid the presence of an un-melted zone between the tracks;
3- Measure the overlap depth (*OD*). The *OD* is the depth of overlap between two adjacent tracks. This distance has to be greater o equal than 1.5 [17] times the value of the layer thickness taken into account during the analysis to ensure a proper remelting of the previous layer;
4- Repeat step 2 for three random overlap regions to assess process variability for the analyzed configuration.

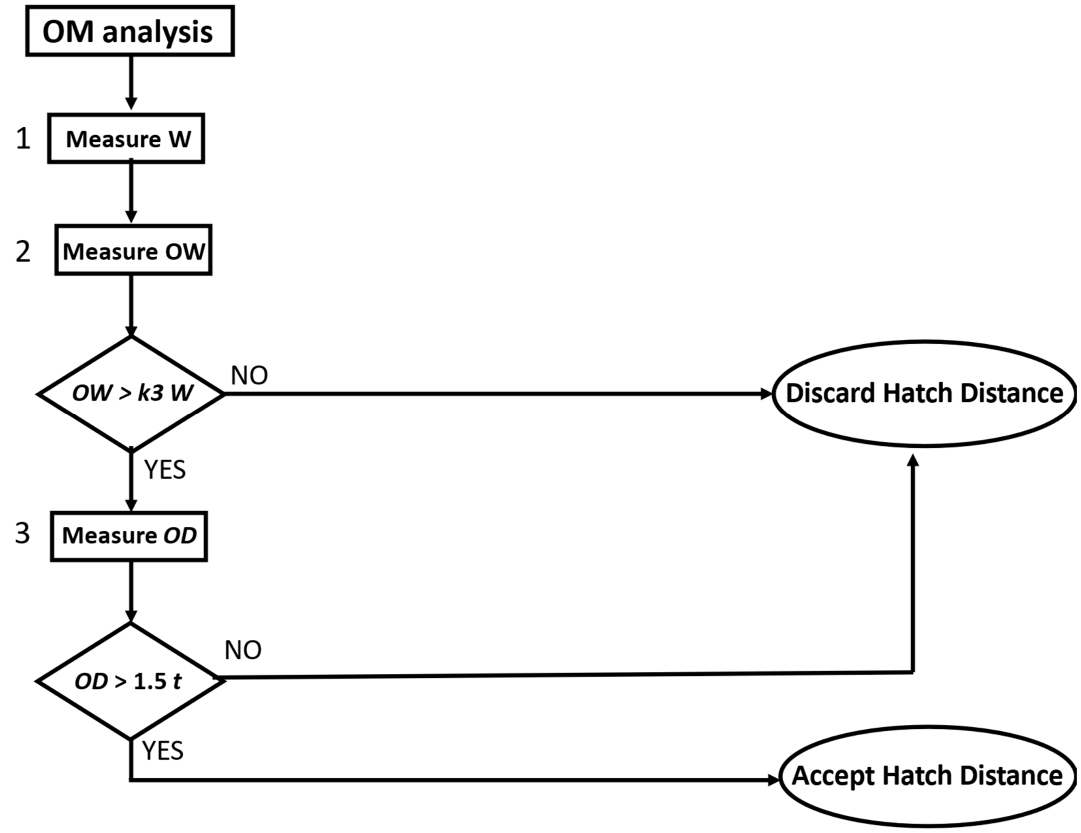

**Figure 10.** Flowchart of multi tracks analysis starting from Optical Microscope (OM) analysis.

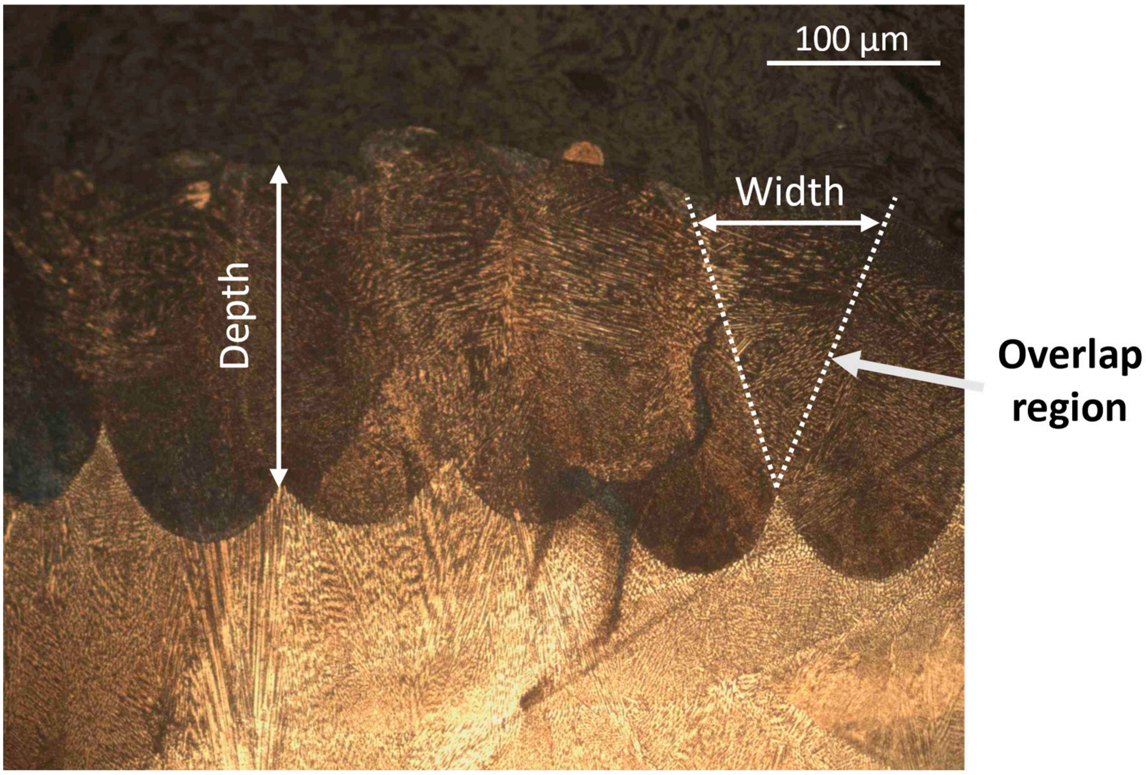

**Figure 11.** Overlap width and depth measurements.

## 3. Results of a Case Study on Inconel 718 Alloy

For the validation of the method, it has been chosen a case study specimen printed in IN718 at a layer thickness of 30 microns (20–60 microns as powder particle size), whose chemical composition, mechanical and thermal properties are shown respectively in Tables 1 and 2.

**Table 1.** Chemical composition of IN718.

| C | Mn | Si | P | S | Cr | Ni | Co | Mo | Nb + Ta | Ti |
|---|---|---|---|---|---|---|---|---|---|---|
| 0.040 | 0.08 | 0.08 | <0.015 | 0.002 | 18.37 | 55.37 | 0.23 | 3.04 | 5.34 | 0.98 |
| **Al** | **B** | **Ta** | **Cu** | **Fe** | **Ca** | **Mg** | **Pb** | **Bi** | **Se** | **Nb** |
| 0.50 | 0.004 | 0.005 | 0.04 | 17.80 | <0.01 | <0.01 | 0.0001 | 0.0001 | <0.001 | 5.33 |

**Table 2.** Mechanical and physical properties of IN718.

| Yield Strength (Mpa) | Tensile Stress (Mpa) | Strain (%) | Elastic Modulus (Gpa) | Thermal Conductivity (W/mK) | Density (kg/m$^3$) |
|---|---|---|---|---|---|
| 1100 | 1310 | 23.3 | 206 | 11.2 | 8470 |

The specimens were printed using the machine Renishaw AM500Q (Renishaw Ltd., Gloucestershire, UK), provided with four ytterbium fiber lasers with a beam wavelength of 1070 nm and a laser focus diameter of 80 µm. The maximum laser power allowed by this machine is 500 Watts for each laser. The preheating temperature of the base plate was set to 170 °C and the oxygen content inside the building chamber was kept constant under 100 ppm by an argon gas flow.

### 3.1. Screening Phase

The parameters widely developed in literature [10,39] for the Inconel 718 at 40 microns of layer thickness were chosen as a reference point.

A 25-point test grid is created to investigate five levels for the Laser Power and Scanning Speed, as shown in Figure 12.

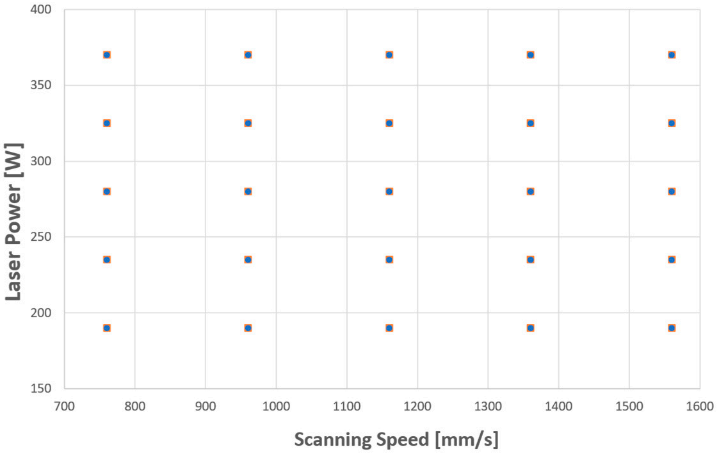

**Figure 12.** Laser power vs. scanning speed grid.

The investigated laser power range is set between 190 and 370 watts. This range was chosen consistent with the parameters already developed in the literature [47] and the laser power limits of the L-PBF machines.

On the other hand, the investigated range for scanning speed is set between 760 and 1560 mm/s in order to evaluate the high productivity zone.

For each grid point, three levels of hatch distance have been investigated. This process parameter has been increased progressively by a quantity equal to 10% with respect to the most common value analyzed in the literature of 0.10 mm [51].

The values of the process parameters assigned to each experiment are shown in Table 3.

**Table 3.** Grid values used in IN718 case study (Layer Thickness 30 microns).

| Sample | Scanning Speed (mm/s) | Laser Power (W) | Hatch Distance (µm) |
|---|---|---|---|
| 1 | 760 | 190 | 0.09/0.10/0.11 |
| 2 | 960 | 190 | 0.09/0.10/0.11 |
| 3 | 1160 | 190 | 0.09/0.10/0.11 |
| 4 | 1360 | 190 | 0.09/0.10/0.11 |
| 5 | 1560 | 190 | 0.09/0.10/0.11 |
| 6 | 760 | 235 | 0.09/0.10/0.11 |
| 7 | 960 | 235 | 0.09/0.10/0.11 |
| 8 | 1160 | 235 | 0.09/0.10/0.11 |
| 9 | 1360 | 235 | 0.09/0.10/0.11 |
| 10 | 1560 | 235 | 0.09/0.10/0.11 |
| 11 | 760 | 280 | 0.09/0.10/0.11 |
| 12 | 960 | 280 | 0.09/0.10/0.11 |
| 13 | 1160 | 280 | 0.09/0.10/0.11 |
| 14 | 1360 | 280 | 0.09/0.10/0.11 |
| 15 | 1560 | 280 | 0.09/0.10/0.11 |
| 16 | 760 | 325 | 0.09/0.10/0.11 |
| 17 | 960 | 325 | 0.09/0.10/0.11 |
| 18 | 1160 | 325 | 0.09/0.10/0.11 |
| 19 | 1360 | 325 | 0.09/0.10/0.11 |
| 20 | 1560 | 325 | 0.09/0.10/0.11 |
| 21 | 760 | 370 | 0.09/0.10/0.11 |
| 22 | 960 | 370 | 0.09/0.10/0.11 |
| 23 | 1160 | 370 | 0.09/0.10/0.11 |
| 24 | 1360 | 370 | 0.09/0.10/0.11 |
| 25 | 1560 | 370 | 0.09/0.10/0.11 |

The geometry of the specimens has been created in commercial CAD software using the dimensions 10 mm × 4 mm × 5 mm (x, y, z).

For this case of study, five single tracks and five multi-tracks for each sub-part have been realized. The track's dimensions are 0.05 × 2 × 0.09 mm (x, y, z).

The CAD file has been exported in STL format, exporting the "body" and the model tracks separately.

The positioning on the base plate and the labelling of the specimens are performed using Materialise Magics 24.1 (Materialise NV, Leuven, Belgium).

The STL outputs have been imported in Renishaw Quantam Software Version 5.3.0.7105 (Renishaw Ltd., Gloucestershire, UK) to assign the process parameters to each specimen according to the values shown in Table 3 after the laser assignment is carried out.

During the printing, all four lasers available on the machine are used.

The printed specimens were removed from the base plate using wire-cutting technology, immersed in an acetone solution and then subjected to ultrasonic cleaning.

A SEM Zeiss SUPRA 55 (Zeiss, Oberkochen, Germany) is used to analyze the specimens' track stability; the images are acquired at 40× magnification with a working distance of 45 mm.

The method described in Section 2 is used to assess the level of stability of the tracks. Table 4 shows the number of section changes and interruptions for each specimen measured. Using this information, the corresponding level of the track's stability and a stability map has been created with the acquired images, as shown in Figure 13.

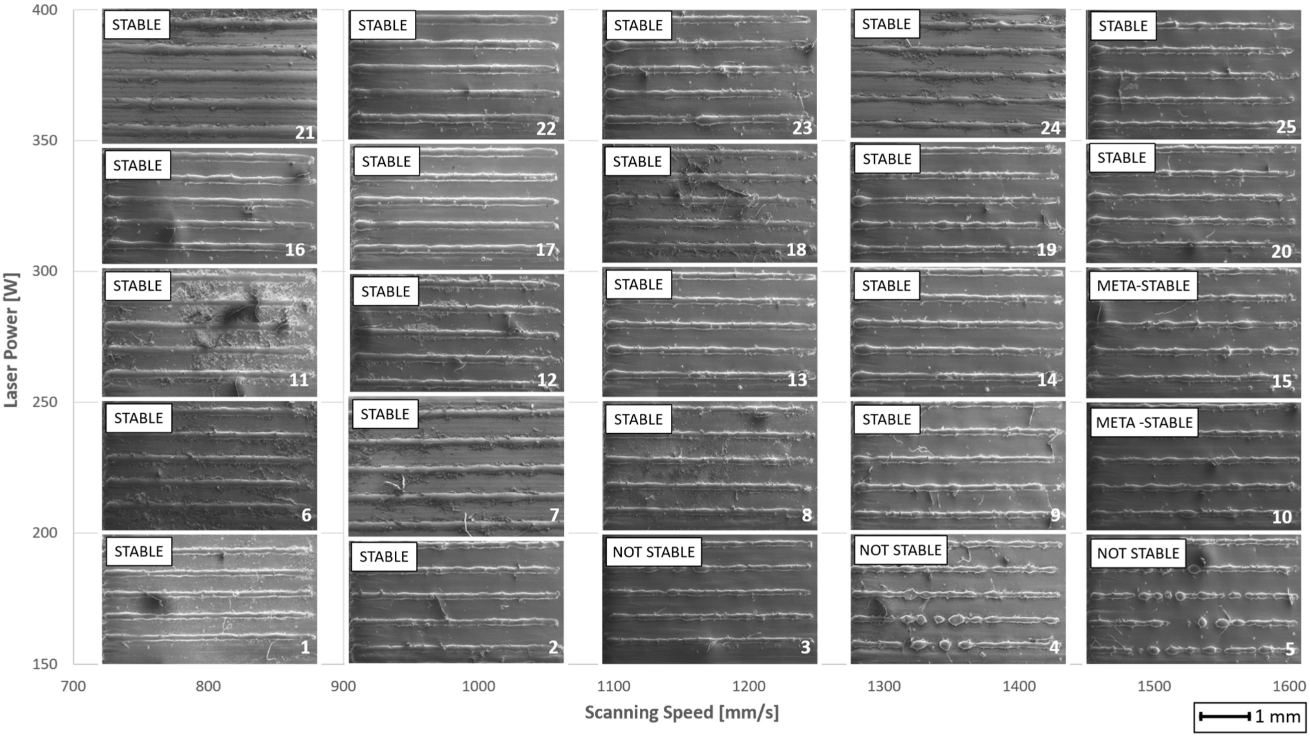

**Figure 13.** Track stability map (number in white indicate the sample).

**Table 4.** Track's stability tracking table.

| Sample | Average Track Shift | Average Interruption | Stability Level |
|---|---|---|---|
| 1 | 0 | 0 | Stable |
| 2 | 0.7 | 0.0 | Stable |
| 3 | 1.0 | 0.3 | Not stable |
| 4 | 1.0 | 1.0 | Not stable |
| 5 | 2.3 | 2.3 | Not stable |
| 6 | 0.0 | 0.0 | Stable |
| 7 | 0.0 | 0.0 | Stable |
| 8 | 0.0 | 0.0 | Stable |
| 9 | 1.0 | 0.0 | Stable |
| 10 | 2.3 | 0.0 | Meta-stable |
| 11 | 0.0 | 0.0 | Stable |
| 12 | 0.0 | 0.0 | Stable |
| 13 | 0.0 | 0.0 | Stable |
| 14 | 0.0 | 0.0 | Stable |
| 15 | 2.1 | 0.0 | Meta-stable |
| 16 | 0.0 | 0.0 | Stable |
| 17 | 0.0 | 0.0 | Stable |

**Table 4.** *Cont.*

| Sample | Average Track Shift | Average Interruption | Stability Level |
|---|---|---|---|
| 18 | 0.0 | 0.0 | Stable |
| 19 | 0.0 | 0.0 | Stable |
| 20 | 0.0 | 0.0 | Stable |
| 21 | 0.0 | 0.0 | Stable |
| 22 | 0.0 | 0.0 | Stable |
| 23 | 0.0 | 0.0 | Stable |
| 24 | 0.0 | 0.0 | Stable |
| 25 | 0.0 | 0.0 | Stable |

### *3.2. Optimization of Laser Power and Scanning Speed*

All specimens are then embedded in a conductive resin and polished to perform subsequent porosity analysis. The analysis has been made in all specimens for the validation of the method; the proper application of the method would have removed all the specimens classified as “not stable” or “meta-stable” according to par.3.1 (Table 4) from the analysis described in this section.

Porosity analysis was performed using Optical Microscope Leica Leitz DMRME (Leica Microsystems GmbH, Wetzlar, Germany) for image acquisition and ImageJ (National Institute of Health, Bethesda, MD, USA) software to calculate the percentage porosity by the evaluation of six fields for each specimen.

Figure 14 shows the images related to the microstructure for the configuration tested with a hatch distance value set to 0.11 mm, while Table 5 shows the results of the porosity analysis performed for all the specimens.

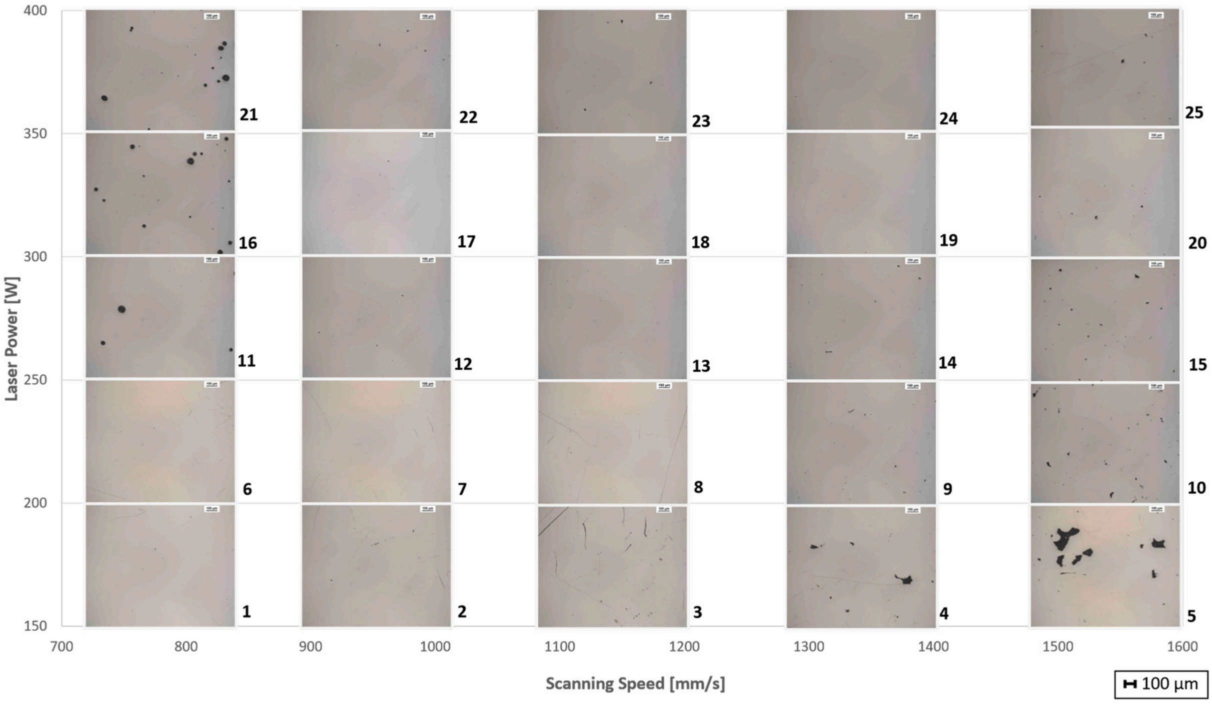

**Figure 14.** Porosity map (hatch distance value 0.11 mm, number in black indicate the sample).

**Table 5.** Porosity tracking table.

| Sample | Scanning Speed (mm/s) | Laser Power (W) | Porosity (%) (HD = 0.09 mm) | | Porosity (%) (HD = 0.10 mm) | | Porosity (%) (HD = 0.11 mm) | |
|---|---|---|---|---|---|---|---|---|
| | | | Avg. | SD | Avg. | SD | Avg. | SD |
| 1 | 760 | 190 | 0.005 | 0.002 | 0.006 | 0.002 | 0.006 | 0.003 |
| 2 | 960 | 190 | 0.009 | 0.005 | 0.009 | 0.002 | 0.017 | 0.010 |
| 3 | 1160 | 190 | 0.049 | 0.012 | 0.066 | 0.013 | 0.092 | 0.027 |
| 4 | 1360 | 190 | 0.066 | 0.015 | 0.088 | 0.014 | 0.333 | 0.147 |
| 5 | 1560 | 190 | 0.140 | 0.036 | 0.373 | 0.205 | 1.490 | 0.768 |
| 6 | 760 | 235 | 0.004 | 0.002 | 0.003 | 0.002 | 0.045 | 0.011 |
| 7 | 960 | 235 | 0.003 | 0.002 | 0.005 | 0.003 | 0.016 | 0.005 |
| 8 | 1160 | 235 | 0.011 | 0.005 | 0.020 | 0.007 | 0.031 | 0.016 |
| 9 | 1360 | 235 | 0.029 | 0.010 | 0.047 | 0.014 | 0.213 | 0.026 |
| 10 | 1560 | 235 | 0.076 | 0.015 | 0.137 | 0.035 | 0.526 | 0.117 |
| 11 | 760 | 280 | 0.072 | 0.018 | 0.002 | 0.002 | 0.024 | 0.011 |
| 12 | 960 | 280 | 0.016 | 0.008 | 0.007 | 0.002 | 0.008 | 0.003 |
| 13 | 1160 | 280 | 0.004 | 0.002 | 0.014 | 0.005 | 0.015 | 0.009 |
| 14 | 1360 | 280 | 0.008 | 0.003 | 0.012 | 0.003 | 0.058 | 0.015 |
| 15 | 1560 | 280 | 0.096 | 0.019 | 0.239 | 0.074 | 0.368 | 0.119 |
| 16 | 760 | 325 | 0.365 | 0.209 | 0.233 | 0.107 | 0.110 | 0.073 |
| 17 | 960 | 325 | 0.010 | 0.005 | 0.008 | 0.003 | 0.012 | 0.006 |
| 18 | 1160 | 325 | 0.006 | 0.004 | 0.015 | 0.007 | 0.016 | 0.006 |
| 19 | 1360 | 325 | 0.011 | 0.004 | 0.012 | 0.005 | 0.038 | 0.010 |
| 20 | 1560 | 325 | 0.018 | 0.007 | 0.029 | 0.009 | 0.063 | 0.014 |
| 21 | 760 | 370 | 0.388 | 0.209 | 0.228 | 0.073 | 0.170 | 0.055 |
| 22 | 960 | 370 | 0.128 | 0.025 | 0.080 | 0.018 | 0.083 | 0.013 |
| 23 | 1160 | 370 | 0.013 | 0.007 | 0.027 | 0.011 | 0.029 | 0.004 |
| 24 | 1360 | 370 | 0.013 | 0.005 | 0.030 | 0.010 | 0.046 | 0.007 |
| 25 | 1560 | 370 | 0.029 | 0.006 | 0.029 | 0.010 | 0.068 | 0.016 |

Subsequently, the specimens are etched using oxalic acid to evaluate the melt pool and the melting regime of the powder.

The images of the melt pool were acquired using an optical microscope, and the melt pool measurements were carried out using NIS-Elements BR software (version 5.30.02).

To assess the melting regime of powder for each specimen, the criterium better described in Section 2.1.4 [17] has been used. The dimensions of the melt pool measured are shown in Table 6. The shape of the melt pool and the calculated melting regime for each configuration are shown in Figure 15 and Table 7, respectively.

**Table 6.** Melt pool dimensions tracking table.

| Sample | Scanning Speed (mm/s) | Laser Power (W) | Depth (µm) | | Width (µm) | |
|---|---|---|---|---|---|---|
| | | | Avg. | SD | Avg. | SD |
| 1 | 760 | 190 | 69.6 | 5.5 | 152.4 | 5.2 |
| 2 | 960 | 190 | 41.8 | 7.4 | 123.4 | 4.8 |
| 3 | 1160 | 190 | 29.4 | 6.3 | 107.2 | 6.5 |

**Table 6.** *Cont.*

| Sample | Scanning Speed (mm/s) | Laser Power (W) | Depth (μm) | | Width (μm) | |
|---|---|---|---|---|---|---|
| | | | Avg. | SD | Avg. | SD |
| 4 | 1360 | 190 | 15.2 | 4.1 | 83.6 | 15.0 |
| 5 | 1560 | 190 | 10.2 | 9.5 | 49.6 | 46.9 |
| 6 | 760 | 235 | 122.2 | 5.2 | 187.8 | 15.1 |
| 7 | 960 | 235 | 78.4 | 9.8 | 135.4 | 9.2 |
| 8 | 1160 | 235 | 61.6 | 10.9 | 116.4 | 6.1 |
| 9 | 1360 | 235 | 51.2 | 4.7 | 108.0 | 2.4 |
| 10 | 1560 | 235 | 35.2 | 6.1 | 100.8 | 6.9 |
| 11 | 760 | 280 | 145.8 | 10.9 | 200.0 | 4.8 |
| 12 | 960 | 280 | 112.6 | 5.7 | 171.8 | 4.1 |
| 13 | 1160 | 280 | 74.8 | 7.9 | 133.0 | 5.6 |
| 14 | 1360 | 280 | 54.8 | 8.0 | 108.6 | 1.7 |
| 15 | 1560 | 280 | 43.0 | 5.0 | 111.2 | 8.7 |
| 16 | 760 | 325 | 199.0 | 17.0 | 196.0 | 15.2 |
| 17 | 960 | 325 | 135.0 | 10.4 | 182.4 | 9.4 |
| 18 | 1160 | 325 | 101.2 | 2.9 | 156.5 | 9.0 |
| 19 | 1360 | 325 | 81.2 | 4.1 | 133.6 | 9.3 |
| 20 | 1560 | 325 | 69.2 | 3.2 | 126.8 | 7.9 |
| 21 | 760 | 370 | 214.6 | 9.9 | 207.8 | 15.2 |
| 22 | 960 | 370 | 154.0 | 6.4 | 200.8 | 8.5 |
| 23 | 1160 | 370 | 115.0 | 7.2 | 162.8 | 6.4 |
| 24 | 1360 | 370 | 71.7 | 3.8 | 132.0 | 11.2 |
| 25 | 1560 | 370 | 75.0 | 6.3 | 130.0 | 9.5 |

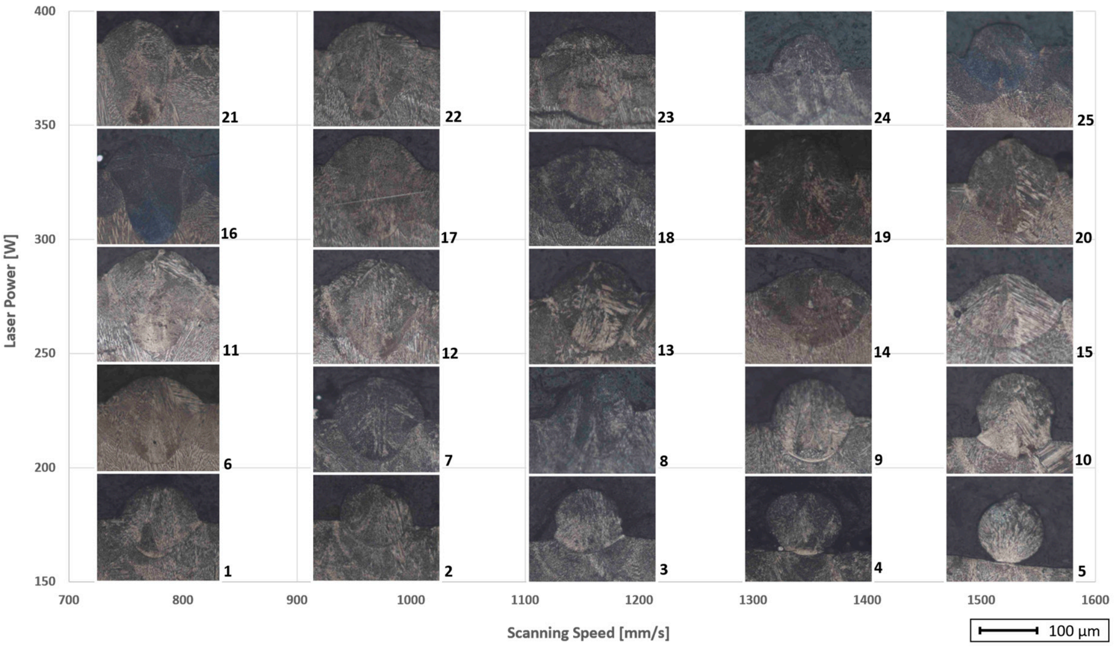

**Figure 15.** Melt pool shape at various levels of laser power and scanning speed (number in black indicate the sample).

**Table 7.** Melt pool dimensions tracking table.

| Sample | Scanning Speed (mm/s) | Laser Power (W) | Depth/Thickness | Width/Depth |
|---|---|---|---|---|
| 1 | 760 | 190 | 2.3 | 2.3 |
| 2 | 960 | 190 | 1.4 | 2.9 |
| 3 | 1160 | 190 | 0.9 | 4.0 |
| 4 | 1360 | 190 | 0.5 | 5.9 |
| 5 | 1560 | 190 | 0.3 | 3.7 |
| 6 | 760 | 235 | 4.1 | 1.5 |
| 7 | 960 | 235 | 2.6 | 1.8 |
| 8 | 1160 | 235 | 2.0 | 2.0 |
| 9 | 1360 | 235 | 1.8 | 2.1 |
| 10 | 1560 | 235 | 1.1 | 3.1 |
| 11 | 760 | 280 | 4.9 | 1.4 |
| 12 | 960 | 280 | 3.8 | 1.5 |
| 13 | 1160 | 280 | 2.4 | 1.8 |
| 14 | 1360 | 280 | 1.9 | 1.9 |
| 15 | 1560 | 280 | 1.4 | 2.1 |
| 16 | 760 | 325 | 6.6 | 1.0 |
| 17 | 960 | 325 | 4.6 | 1.4 |
| 18 | 1160 | 325 | 3.4 | 1.5 |
| 19 | 1360 | 325 | 2.7 | 1.6 |
| 20 | 1560 | 325 | 2.3 | 1.8 |
| 21 | 760 | 370 | 7.1 | 1.0 |
| 22 | 960 | 370 | 5.1 | 1.3 |
| 23 | 1160 | 370 | 3.9 | 1.4 |
| 24 | 1360 | 370 | 1.8 | 1.9 |
| 25 | 1560 | 370 | 2.5 | 1.8 |

### *3.3. Optimization of Hatch Distance*

Multi-tracks analysis is carried out on all the specimens following the criteria described above in Section 2.2.2. The analysis has been made in all specimens for validation for the paper's aim; the proper application of the method would have focused the optimization of hatch distance on the configuration selected in the previous phases as best according to the purpose of the research.

In Table 8, measurements of overlapping zone dimensions were tracked for each specimen and the possible presence of flaws in this zone was registered in Table 9.

**Table 8.** Multi-tracks melt pool dimensions tracking table. The measure of each sample is referred to 0.09/0.10/0.11 mm as hatch distance I/II/III, respectively. SS and # mean scan speed and sample number respectively.

| # | SS (mm/s) | P (W) | Overlap Width Average (μm) | | | | | | Overlap Depth Average (μm) | | | | | | Width Tracks Average (μm) | | | | | |
|---|---|---|---|---|---|---|---|---|---|---|---|---|---|---|---|---|---|---|---|---|
| | | | I | | II | | III | | I | | II | | III | | I | | II | | III | |
| | | | Avg. | SD | Avg. | SD | Avg. | SD | Avg. | SD | Avg. | SD | Avg. | SD | Avg. | SD | Avg. | SD | Avg. | SD |
| 1 | 760 | 190 | 80 | 7 | 69 | 13 | 60 | 15 | 101 | 11 | 89 | 8 | 66 | 16 | 127 | 10 | 141 | 22 | 134 | 6 |
| 2 | 960 | 190 | 45 | 21 | 21 | 19 | 12 | 20 | 51 | 30 | 18 | 18 | 10 | 17 | 111 | 5 | 102 | 9 | 109 | 7 |
| 3 | 1160 | 190 | 25 | 5 | 10 | 9 | 6 | 10 | 43 | 10 | 11 | 11 | 13 | 22 | 109 | 53 | 97 | 6 | 107 | 8 |

**Table 8.** *Cont.*

| # | SS (mm/s) | P (W) | Overlap Width Average (μm) | | | | | | Overlap Depth Average (μm) | | | | | | Width Tracks Average (μm) | | | | | |
|---|---|---|---|---|---|---|---|---|---|---|---|---|---|---|---|---|---|---|---|---|
| | | | I | | II | | III | | I | | II | | III | | I | | II | | III | |
| | | | Avg. | SD | Avg. | SD | Avg. | SD | Avg. | SD | Avg. | SD | Avg. | SD | Avg. | SD | Avg. | SD | Avg. | SD |
| 4 | 1360 | 190 | 12 | 11 | 7 | 12 | 0 | 0 | 16 | 16 | 6 | 11 | 0 | 0 | 89 | 15 | 93 | 11 | 98 | 12 |
| 5 | 1560 | 190 | 15 | 25 | 0 | 0 | 0 | 0 | 0 | 0 | 0 | 0 | 0 | 0 | 91 | 6 | 88 | 2 | 92 | 3 |
| 6 | 760 | 235 | 92 | 8 | 86 | 7 | 83 | 7 | 160 | 5 | 149 | 10 | 123 | 14 | 176 | 3 | 177 | 13 | 180 | 15 |
| 7 | 960 | 235 | 88 | 10 | 74 | 7 | 71 | 8 | 86 | 12 | 92 | 12 | 90 | 5 | 134 | 2 | 135 | 11 | 137 | 5 |
| 8 | 1160 | 235 | 68 | 14 | 55 | 11 | 36 | 8 | 78 | 3 | 63 | 13 | 55 | 12 | 117 | 7 | 114 | 2 | 116 | 6 |
| 9 | 1360 | 235 | 32 | 5 | 12 | 13 | 9 | 10 | 33 | 1 | 17 | 10 | 15 | 14 | 95 | 6 | 100 | 1 | 104 | 5 |
| 10 | 1560 | 235 | 13 | 12 | 13 | 22 | 0 | 0 | 17 | 15 | 8 | 13 | 0 | 0 | 91 | 2 | 92 | 6 | 100 | 6 |
| 11 | 760 | 280 | 110 | 2 | 99 | 9 | 97 | 9 | 161 | 22 | 155 | 17 | 143 | 35 | 170 | 6 | 170 | 13 | 170 | 10 |
| 12 | 960 | 280 | 84 | 3 | 76 | 8 | 65 | 12 | 127 | 6 | 120 | 11 | 117 | 24 | 156 | 12 | 150 | 10 | 156 | 11 |
| 13 | 1160 | 280 | 69 | 7 | 56 | 12 | 54 | 9 | 98 | 12 | 83 | 10 | 73 | 16 | 121 | 11 | 125 | 12 | 127 | 6 |
| 14 | 1360 | 280 | 52 | 3 | 35 | 6 | 22 | 7 | 89 | 13 | 50 | 6 | 35 | 16 | 115 | 1 | 107 | 4 | 113 | 2 |
| 15 | 1560 | 280 | 27 | 3 | 15 | 14 | 0 | 0 | 29 | 2 | 20 | 20 | 0 | 0 | 98 | 4 | 99 | 6 | 101 | 6 |
| 16 | 760 | 325 | 139 | 11 | 132 | 4 | 117 | 20 | 218 | 13 | 203 | 21 | 199 | 44 | 193 | 42 | 197 | 9 | 201 | 30 |
| 17 | 960 | 325 | 125 | 12 | 109 | 17 | 92 | 9 | 143 | 14 | 134 | 17 | 121 | 12 | 175 | 13 | 174 | 2 | 178 | 3 |
| 18 | 1160 | 325 | 78 | 2 | 78 | 10 | 69 | 13 | 111 | 6 | 105 | 4 | 100 | 17 | 139 | 9 | 144 | 4 | 140 | 5 |
| 19 | 1360 | 325 | 78 | 9 | 50 | 5 | 43 | 14 | 104 | 11 | 83 | 12 | 52 | 15 | 130 | 6 | 130 | 12 | 123 | 10 |
| 20 | 1560 | 325 | 54 | 8 | 29 | 9 | 20 | 17 | 70 | 14 | 31 | 15 | 19 | 16 | 114 | 14 | 107 | 4 | 111 | 10 |
| 21 | 760 | 370 | 139 | 22 | 140 | 13 | 116 | 5 | 231 | 29 | 212 | 33 | 201 | 42 | 207 | 43 | 209 | 54 | 227 | 40 |
| 22 | 960 | 370 | 135 | 20 | 132 | 12 | 116 | 17 | 168 | 19 | 155 | 13 | 150 | 26 | 184 | 22 | 186 | 17 | 195 | 15 |
| 23 | 1160 | 370 | 102 | 17 | 96 | 6 | 82 | 12 | 126 | 17 | 119 | 15 | 116 | 19 | 153 | 7 | 161 | 9 | 165 | 9 |
| 24 | 1360 | 370 | 86 | 8 | 64 | 9 | 58 | 6 | 90 | 10 | 83 | 7 | 40 | 11 | 135 | 8 | 126 | 6 | 120 | 6 |
| 25 | 1560 | 370 | 71 | 8 | 46 | 10 | 34 | 16 | 93 | 14 | 68 | 27 | 29 | 7 | 117 | 18 | 118 | 19 | 117 | 5 |

**Table 9.** Multi-tracks melt pool dimensions tracking table. The measure of each sample is referred to 0.09/0.10/0.11 mm as hatch distance I/II/III, respectively. The abbreviations NR and NO mean, respectively, “Not Remelting” and “Not Overlap”, SS and # mean scan speed and sample number.

| # | Scan Speed (mm/s) | Power (W) | Remelting Depth | | | Overlap Threshold | | |
|---|---|---|---|---|---|---|---|---|
| | | | I | II | III | I | II | III |
| 1 | 760 | 190 | Ok | Ok | Ok | Ok | Ok | Ok |
| 2 | 960 | 190 | Ok | NR | NR | Ok | Ok | NO |
| 3 | 1160 | 190 | NR | NR | NR | Ok | NO | NO |
| 4 | 1360 | 190 | NR | NR | NR | NO | NO | NO |
| 5 | 1560 | 190 | NR | NR | NR | NO | NO | NO |
| 6 | 760 | 235 | Ok | Ok | Ok | Ok | Ok | Ok |
| 7 | 960 | 235 | Ok | Ok | Ok | Ok | Ok | Ok |
| 8 | 1160 | 235 | Ok | Ok | Ok | Ok | Ok | Ok |

**Table 9.** *Cont.*

| # | Scan Speed (mm/s) | Power (W) | Remelting Depth | | | Overlap Threshold | | |
|---|---|---|---|---|---|---|---|---|
| | | | I | II | III | I | II | III |
| 9 | 1360 | 235 | NR | NR | NR | Ok | NO | NO |
| 10 | 1560 | 235 | NR | NR | NR | NO | NO | NO |
| 11 | 760 | 280 | Ok | Ok | Ok | Ok | Ok | Ok |
| 12 | 960 | 280 | Ok | Ok | Ok | Ok | Ok | Ok |
| 13 | 1160 | 280 | Ok | Ok | Ok | Ok | Ok | Ok |
| 14 | 1360 | 280 | Ok | Ok | NR | Ok | Ok | NO |
| 15 | 1560 | 280 | NR | NR | NR | Ok | NO | NO |
| 16 | 760 | 325 | Ok | Ok | Ok | Ok | Ok | Ok |
| 17 | 960 | 325 | Ok | Ok | Ok | Ok | Ok | Ok |
| 18 | 1160 | 325 | Ok | Ok | Ok | Ok | Ok | Ok |
| 19 | 1360 | 325 | Ok | Ok | Ok | Ok | Ok | Ok |
| 20 | 1560 | 325 | Ok | NR | NR | Ok | Ok | NO |
| 21 | 760 | 370 | Ok | Ok | Ok | Ok | Ok | Ok |
| 22 | 960 | 370 | Ok | Ok | Ok | Ok | Ok | Ok |
| 23 | 1160 | 370 | Ok | Ok | Ok | Ok | Ok | Ok |
| 24 | 1360 | 370 | Ok | Ok | NR | Ok | Ok | Ok |
| 25 | 1560 | 370 | Ok | Ok | NR | Ok | Ok | Ok |

In Figure 16, it is possible to see an example of the effect of the variation of hatch distance on the geometric dimensions of the overlap area.

| **Sample number** | **22-a** | **22-b** | **22-c** |
|---|---|---|---|
| **Layer Thickness (mm)** | 0.03 | 0.03 | 0.03 |
| **Laser Power (W)** | 370 | 370 | 370 |
| **Scanning Speed (mm/s)** | 960 | 960 | 960 |
| **Hatch distance (µm)** | 90 | 100 | 110 |
| **Overlap depth (µm)** | 168 | 155 | 150 |
| **Overlap width (µm)** | 135 | 132 | 116 |
| **Tracks average width (µm)** | 184 | 186 | 195 |

**Figure 16.** Effect of variation of hatch distance on overlap region dimensions.

## 4. Discussion

Based on the results shown in Tables 5–7, the values of factor “*k*1” and “*k*2” have been chosen as 3 and 2, respectively. These specific values for factors “*k*1” and “*k*2” are chosen by the evaluation of porosity and melt pool analysis results. In particular, it can be observed that configurations 10 and 15, considered “meta-stable” for this case of study, have relatively high porosity values and present a depth/layer thickness ratio that indicates the presence of a lack of fusion regime. More specifically, for configuration number 10 the melting regime is entirely in lack of fusion mode; for configuration number 15, the melting regime is not so far from conductive melting mode.

Moreover, from the results of the porosity analysis (Table 5), it is possible to observe that the specimens with tracks previously evaluated as "not stable" or "meta-stable" present the highest values of porosity level for each value of hatch distance tested. In contrast, specimens 11, 16 and 21 are affected by spherical defects that indicate the presence of the Keyhole melting mode of powder. In this case, it is not possible to detect this phenomenon by analyzing the stability level of tracks because, as shown in Figure 16, the tracks printed on specimens number 11, 16 and 21 are evaluated as "stable". Furthermore, it can be observed that the specimens found to be most unstable through the proposed approach show a high variability of porosity correlated to the high average porosity values (Pearson correlation 0,97, $p$-value < 0,01), probably as an effect of an unstable process.

After melt pool analysis (Table 6), it is possible to state that even in terms of melt pool shape, the unstable tracks are affected by a lack of fusion regime. This result is of great interest because it directly correlates the track instability to the lack of fusion regime on the sample. On the contrary, based on the results obtained so far, the level of stability of the tracks has no correlation with the presence or absence of the keyhole regime. Consequently, the presence of the keyhole melting regime is not detectable from an assessment of the stability of the track. This aspect is not a limitation for applications of the method if the purpose of the activity is to develop highly productive parameters; in this case, the keyhole region will be discarded a priori for the low productivity values.

Based on the results of this case study, the value suggested by Johnson et al. [38] for the calculation of the lack of fusion in terms of depth/layer thickness ratio could be reduced from 1.5 to 1.4.

Using this method for the material characterization allows for speeding up optimal process parameters development, maintaining sufficient information content on material microstructure in terms of porosity and melt pool measure.

Based on the results of this study, it is to emphasize that in order to develop parameters that assure high productivity but at the same time stable and robust process, the use of the proposed screening method is extremely relevant. In fact, in this case, it is suggested to choose among samples with stable tracks the one that presents the highest value of scanning speed and that is surrounded by samples with stable or meta-stable tracks.

Thus, following this path, the proposed method becomes highly efficient and helpful if the goal is to investigate only points at high-velocity values and obtain maximum productivity, and no printability map is required. In this case, being far from the zone of keyhole melt pool formation, the specimens with tracks will be stable and not be affected by the phenomena of not properly melting; in this case, the melt pool formation will be governed by the conduction phenomenon.

Considering this case study results, it would have been sufficient to perform a porosity and melt pool analysis only on configurations number 14 and 19, resulting among the stable tracks specimens to be ones with the highest value of scanning speed. So, in this case, the number of specimens to be analyzed would have been reduced by 92%. Then, for the configuration selected as the better of the two analyzed, a sensitivity analysis can be carried out to assess the stability of the surroundings of this configuration in laser power-scanning speed space; in particular, its robustness consistent with process drift phenomena such as laser drift can be evaluated.

Relative to hatch distance optimization, using multi-tracks analysis results, it is possible to notice that for the specimens with a higher value of scanning speed with the same laser power, the dimensions of the depth and the width of the overlap zone between the tracks decrease as the hatch distance value increases (Figure 15).

An example of this is represented by configuration number 14 (see Table 6 for further details concerning the parameters), in which the increase of hatch distance leads to an overlap zone between the tracks not adequate in terms of *OD* and *OW*.

The coefficient "$k3$" used to assess the *OW* adequacy (i.e., enough overlap between adjacent tracks) has been evaluated at 0.2, considering the porosity measurements (Table 5). This value is able to identify conditions critical for porosity level and, on the other hand, allows the overcoming of the screening phase to the configurations characterized by an acceptable porosity level. Some of these configurations will be analyzed in more detail once the screening phase is completed. It is essential to point out that the OW results for configurations already discarded in the previous screening phase of the method proposed are not significant.

Consequently, using the multi-tracks analysis, it is possible to evaluate quickly based on the geometric dimensions of the overlap area (*OD* and *OW*) if the hatch distance value selected for the configuration of laser power and scanning speed investigated is acceptable or not (Tables 8 and 9).

So, this method is an effective and easy-to-apply tool to optimize the hatch distance parameter starting from a direct analysis of the overlap zone between tracks.

Compared to classical methods, which do not make use of multi-tracks printing and for which the optimization of hatch distance value is carried out indirectly by porosity analysis, this method allows having direct and accurate information of the maximum admitted hatch distance value as a function of the dimensions of the overlap area between the tracks.

The calculated values for "$k1$", "$k2$", and "$k3$" identified in this case study will need to be verified for different layer thicknesses for IN718 and other nickel-based superalloys. Most probably, the values could be confirmed as nickel-based superalloys printed by L-PBF process is similar in printability properties [22].

## 5. Conclusions

The method proposed in this paper can effectively speed up material characterization for the AM L-PBF technique increasingly frequent due to the continuously evolving technology (e.g., changes in the number of lasers used, process parameters, and introduction of materials with higher scanning speed).

Reducing the number of specimens to be analyzed is a function of the requirements for the case study to be carried out. Relative to this case study, if the definition of a complete printability map for the material was required, the reduction in the number of specimens to be analyzed would have been 25%. On the contrary, if only the stable configurations characterized by higher productivity had been analyzed, the reduction would have been more than 90%.

This method turns out to be all the more effective, the more detailed the analysis to be performed; that is, for a large number of levels to be investigated for laser power and scanning speed, the screening phase acquires greater effectiveness and importance. In addition, the ability to investigate numerous configurations in laser power, scanning speed and hatch distance space allows the identification of a robust printability map for a material.

At posteriori analysis of the experimental results in the case study on IN718 presented in the paper confirms the proposed method's potential for a more time and cost-effective parameter development in LPBF. In fact, the obtained results make it possible to state that this method provides accurate information on the powder melting regime. The method allows fast screening and optimization of the most influent process parameters used during the printing.

In particular, the printing of multi-tracks allows the direct optimization of the process parameter hatch distance previously optimized indirectly through porosity analysis; in this case, instead, it is possible to directly correlate the maximum allowed hatch distance value to easily measurable geometric dimensions, thus providing sufficient stable and reproducible criteria.

Further case studies will be carried out to evaluate the possible analysis of meta-stable configurations and the method's robustness to changing boundary conditions, such as the type of material and layer thickness investigated.

**Author Contributions:** Conceptualization, A.G., N.B. and F.C.; investigation, A.G., N.B. and M.P.; resources, F.C., M.P. and P.C.; methodology, A.G. and N.B.; validation, F.C. and M.P.; formal analysis, A.G. and N.B.; visualization, A.G. and N.B.; data curation, A.G. and N.B.; writing—original draft, A.G. and N.B.; writing—review and editing, A.G., N.B. and G.A.; supervision, G.A. and P.C. All authors have read and agreed to the published version of the manuscript.

**Funding:** This research received no external funding.

**Data Availability Statement:** The data presented in this study are available on request from the corresponding author.

**Conflicts of Interest:** The authors declare no conflict of interest.

## References

1. Wang, Z.; Guan, K.; Gao, M.; Li, X.; Chen, X.; Zeng, X. The microstructure and mechanical properties of deposited-IN718 by selective laser melting. *J. Alloys Compd.* **2012**, *513*, 518–523. [CrossRef]
2. Das, S. Physical aspects of process control in selective laser sintering of metals. *Adv. Eng. Mater.* **2003**, *5*, 701–711. [CrossRef]
3. Osakada, K.; Shiomi, M. Flexible manufacturing of metallic products by selective laser melting of powder. *Int. J. Mach. Tools Manuf.* **2006**, *46*, 1188–1193. [CrossRef]
4. Kruth, J.P.; Mercelis, P.; Van Vaerenbergh, J.; Froyen, L.; Rombouts, M. Binding mechanisms in selective laser sintering and selective laser melting. *Rapid Prototyp. J.* **2005**, *11*, 26–36. [CrossRef]
5. Yadroitsev, I.; Gusarov, A.; Yadroitsava, I.; Smurov, I. Single track formation in selective laser melting of metal powders. *J. Mater. Process. Technol.* **2010**, *210*, 1624–1631. [CrossRef]
6. Gu, D.D.; Meiners, W.; Wissenbach, K.; Poprawe, R. Laser additive manufacturing of ceramic components: Materials, processes, and mechanisms. *Laser Addit. Manuf. Mater. Des. Technol. Appl.* **2016**, *6608*, 163–180.
7. Smith, J.; Xiong, W.; Yan, W.; Lin, S.; Cheng, P.; Kafka, O.L.; Wagner, G.J.; Cao, J.; Liu, W.K. Linking process, structure, property, and performance for metal-based additive manufacturing: Computational approaches with experimental support. *Comput. Mech.* **2016**, *57*, 583–610. [CrossRef]
8. Metelkova, J.; Kinds, Y.; Kempen, K.; De Formanoir, C.; Witvrouw, A.; Van Hooreweder, B. On the influence of laser defocusing in Selective Laser Melting of 316L. *Addit. Manuf.* **2018**, *23*, 161–169. [CrossRef]
9. Ceccanti, F.; Giorgetti, A.; Arcidiacono, G.; Citti, P. Laser Powder Bed Fusion: A Review on the Design Constraints. *IOP Conf. Ser. Mater. Sci. Eng.* **2021**, *1038*, 012065. [CrossRef]
10. Singh, S.N.; Chowdhury, S.; Nirsanametla, Y.; Deepati, A.K.; Prakash, C.; Singh, S.; Wu, L.Y.; Zheng, H.Y.; Pruncu, C. A Comparative Analysis of Laser Additive Manufacturing of High Layer Thickness Pure Ti and Inconel 718 Alloy Materials Using Finite Element Method. *Materials* **2021**, *14*, 876. [CrossRef]
11. Mahmoud, D.; Magolon, M.; Boer, J.; Elbestawi, M.A.; Mohammadi, M.G. Applications of Machine Learning in Process Monitoring and Controls of L-PBF Additive Manufacturing: A Review. *Appl. Sci.* **2021**, *21*, 11910. [CrossRef]
12. Achillas, C.; Tzetzis, D.; Raimondo, M.O. Alternative production strategies based on the comparison of additive and traditional manufacturing technologies. *Int. J. Prod. Res.* **2017**, *55*, 3497–3509. [CrossRef]
13. Ciappi, A.; Giorgetti, A.; Ceccanti, F.; Canegallo, G. Technological and economical consideration for turbine blade tip restoration through metal deposition technologies. *Proc. Inst. Mech. Eng. Part C J. Mech. Eng. Sci.* **2021**, *235*, 1741–1758. [CrossRef]
14. Cobbinah, P.V.; Nzeukou, R.A.; Onawale, O.T.; Matizamhuka, W.R. Laser Powder Bed Fusion of Potential Superalloys: A Review. *Metals* **2021**, *11*, 58. [CrossRef]
15. Abd-Elaziem, W.; Elkatatny, S.; Abd-Elaziem, A.; Khedr, M.; El-baky, M.A.A.; Hassan, M.A.; Abu-Okail, M.; Mohammed, M.; Järvenpää, A.; Allam, T.; et al. On the current research progress of metallic materials fabricated by laser powder bed fusion process: A review. *J. Mater. Res. Technol.* **2022**, *20*, 681–707. [CrossRef]
16. Ceccanti, F.; Giorgetti, A.; Citti, P. A support structure design strategy for laser powder bed fused parts. *Procedia Struct. Integr.* **2019**, *24*, 667–679. [CrossRef]
17. Blakey-Milner, B.; Gradl, P.; Snedden, G.; Brooks, M.; Pitot, J.; Lopez, E.; Leary, M.; Berto, F.; Du Plessis, A. Metal additive manufacturing in aerospace: A review. *Mater. Des.* **2021**, *209*, 110008. [CrossRef]
18. Khan, H.M.; Karabulut, Y.; Kitay, O.; Kaynak, Y.; Jawahir, I.S. Influence of the post-processing operations on surface integrity of metal components produced by laser powder bed fusion additive manufacturing: A review. *Mach. Sci. Technol.* **2021**, *25*, 118–176. [CrossRef]
19. Mostafaei, A.; Zhao, C.; He, Y.; Ghiaasiaan, S.R.; Shi, B.; Shao, S.; Shamsaei, N.; Wu, Z.; Kouraytem, N.; Sun, T.; et al. Defects and anomalies in powder bed fusion metal additive manufacturing. *Curr. Opin. Solid State Mater. Sci.* **2022**, *26*, 100974. [CrossRef]
20. Makona, N.W.; Yadroitsava, I.; Moller, H.; Tlotleng, M.; Yadroitsev, I. Evaluation of single tracks of 17-4PH steel manufactured at different power densities and scanning speeds by selective laser melting. *S. Afr. J. Ind. Eng.* **2016**, *27*, 210–218. [CrossRef]
21. Liu, X.; Wang, K.; Hu, P.; He, X.; Yan, B.; Zhao, X. Formability, Microstructure and Properties of Inconel 718 Superalloy Fabricated by Selective Laser Melting Additive Manufacture Technology. *Materials* **2021**, *14*, 991. [CrossRef] [PubMed]

22. Panwisawas, C.; Gong, Y.; Tang, Y.T.; Reed, R.C.; Shinjo, J. Additive manufacturability of superalloys: Process-induced porosity, cooling rate and metal vapour. *Addit. Manuf.* **2021**, *47*, 102339. [CrossRef]
23. Abedi, H.R.; Hanzaki, A.Z.; Azami, M.; Kahnooji, M.; Rahmatabadi, D. The high temperature flow behavior of additively manufactured Inconel 625 superalloy. *Mater. Res. Express* **2019**, *6*, 116514. [CrossRef]
24. Yuhua, C.; Yuqing, M.; Weiwei, L.; Peng, H. Investigation of welding crack in micro-laser welded NiTiNb shape memory alloy and Ti6Al4V alloy dissimilar metals joints. *Opt. Laser Technol.* **2017**, *91*, 197–202. [CrossRef]
25. Xie, J.; Chen, Y.; Yin, L.; Zhang, T.; Wang, S.; Wang, L. Microstructure and mechanical properties of ultrasonic spot welding TiNi/Ti6Al4V dissimilar materials using pure Al coating. *J. Manuf. Process.* **2021**, *64*, 473–480. [CrossRef]
26. Deng, H.; Chen, Y.; Jia, Y.; Pang, Y.; Zhang, T.; Wang, S.; Yin, L. Microstructure and mechanical properties of dissimilar NiTi/Ti6Al4V joints via back-heating assisted friction stir welding. *J. Manuf. Process.* **2021**, *64*, 379–391. [CrossRef]
27. Kan, W.H.; Chiu, L.N.S.; Lim, C.V.S.; Zhu, Y.; Tian, Y.; Jiang, D.; Huang, A. A critical review on the effects of process-induced porosity on the mechanical properties of alloys fabricated by laser powder bed fusion. *J. Mater. Sci.* **2022**, *57*, 9818–9865. [CrossRef]
28. Oliveira, J.P.; Santos, T.G.; Miranda, R.M. Revisiting fundamental welding concepts to improve additive manufacturing: From theory to practice. *Prog. Mater. Sci.* **2020**, *107*, 100590. [CrossRef]
29. Mukherjee, T.; Zuback, J.S.; De, A.; DebRoy, T. Printability of alloys for additive manufacturing. *Sci. Rep.* **2016**, *6*, 19717. [CrossRef]
30. Oliveira, J.P.; LaLonde, A.D.; Ma, J. Processing parameters in laser powder bed fusion metal additive manufacturing. *Mater. Des.* **2020**, *193*, 108762. [CrossRef]
31. Giorgetti, A.; Ceccanti, F.; Citti, P.; Ciappi, A.; Arcidiacono, G. Axiomatic Design of Test Artifact for Laser Powder Bed Fusion Machine Capability Assessment. *MATEC Web Conf.* **2019**, *301*, 00006. [CrossRef]
32. Giorgetti, A.; Ceccanti, F.; Kemble, S.; Arcidiacono, G.; Citti, P. _L-PBF Machine Capability Monitoring through an Axiomatic Designed Test Artifact. *Designs forthcoming*.
33. Ahmadi, M.; Tabary, S.B.; Rahmatabadi, D.; Ebrahimi, M.S.; Abrinia, K.; Hashemi, R. Review of Selective Laser Melting of Magnesium Alloys: Advantages, Microstructure and Mechanical Characterizations, Defects, Challenges, and Applications. *J. Mater. Res. Technol.* **2022**, *19*, 1537–1562. [CrossRef]
34. Li, S.; Xiao, H.; Liu, K.; Xiao, W.; Li, Y.; Han, X.; Song, J.M.L. Melt-pool motion, temperature variation and dendritic morphology of Inconel 718 during pulsed- and continuous-wave laser additive manufacturing: A comparative study. *Mater. Des.* **2017**, *119*, 351–360. [CrossRef]
35. Makona, N.W.; Yadroitsava, I.; Moller, H.; Yadroitsev, I. Characterization of 17-4PH single tracks produced at different parametric conditions towards increased productivity of LPBF systems—The effect of laser power and spot size upscaling. *Metals* **2018**, *8*, 475. [CrossRef]
36. Manvatkar, V.; De, A.; Debroy, T. Heat transfer and material flow during laser assisted multi-layer additive manufacturing. *J. Appl. Phys.* **2014**, *116*, 124905. [CrossRef]
37. Johnson, L.; Mahmoudi, M.; Zhang, B.; Seede, R.; Huang, X.; Maier, J.T.; Maier, H.J.; Karaman, I.; Elwany, A.; Arróyave, R. Assessing printability maps in additive manufacturing of metal alloys. *Acta Mater.* **2019**, *176*, 199–210. [CrossRef]
38. Tenbrock, C.; Fischer, F.G.; Wissenbach, K.; Schleifenbaum, J.H.; Wagenblast, P.; Meiners, W.; Wagner, J. Influence of keyhole and conduction mode melting for top-hat shaped beam profiles in laser powder bed fusion. *J. Mater. Process. Technol.* **2020**, *278*, 116514. [CrossRef]
39. King, W.A.; Barth, H.D.; Castillo, V.M.; Gallegos, G.F.; Gibbs, J.W.; Hahn, D.E.; Kamath, C.; Rubenchik, A.M. Observation of keyhole-mode laser melting in laser powder-bed fusion additive manufacturing. *J. Mater. Process. Technol.* **2014**, *214*, 2915–2925. [CrossRef]
40. Tian, Y.; Tomus, D.; Rometsch, P.; Wu, X. Influences of processing parameters on surface roughness of Hastelloy X produced by selective laser melting. *Addit. Manuf.* **2017**, *13*, 103–112. [CrossRef]
41. Ning, J.; Wang, W.; Zamorano, B.; Liang, S.Y. Analytical modeling of lack-of-fusion porosity in metal additive manufacturing. *Appl. Phys.* **2019**, *125*, 797. [CrossRef]
42. Mukherjee, T.; DebRoy, T. Mitigation of lack of fusion defects in powder bed fusion additive manufacturing. *J. Manuf. Process.* **2018**, *36*, 442–449. [CrossRef]
43. Leicht, A.; Fischer, M.; Klement, U.; Nyborg, L.; Hryha, E. Increasing the Productivity of Laser Powder Bed Fusion for Stainless Steel 316L through Increased Layer Thickness. *J. Mater. Eng. Perform.* **2021**, *30*, 575–584. [CrossRef]
44. Childs, T.H.C.; Hauser, C.; Badrossamay, M. Mapping and Modelling Single Scan Track Formation in Direct Metal Selective Laser Melting. *CIRP Ann.* **2004**, *53*, 191–194. [CrossRef]
45. Guo, Y.; Jia, L.; Kong, B.; Wang, N.; Zhang, H. Single track and single layer formation in selective laser melting of niobium solid solution alloy. *Chin. J. Aeronaut.* **2018**, *31*, 860–866. [CrossRef]
46. Shrestha, S.; Chou, K. Single track scanning experiment in laser powder bed fusion process. *Procedia Manuf.* **2018**, *26*, 857–864. [CrossRef]
47. Balbaa, M.; Mekhiel, S.; Elbestawi, M.; McIsaac, J. On Selective laser melting of Inconel 718: Densification, surface roughness, and residual stresses. *Mater. Des.* **2020**, *193*, 108818. [CrossRef]
48. Yadroitsava, I.; Els, J.; Booysen, G.; Yadroitsev, I. Peculiarities of single track formation from Ti6AL4V alloy at different laser power densities by selective laser melting. *S. Afr. J. Ind. Eng.* **2015**, *26*, 86–95. [CrossRef]

49. Zheng, H.; Wang, Y.; Xie, Y.; Yang, S.; Hou, R.; Ge, Y.; Lang, L.; Gong, S.; Li, H. Observation of Vapor Plume Behavior and Process Stability at Single-Track and Multi-Track Levels in Laser Powder Bed Fusion Regime. *Metals* **2021**, *11*, 937. [CrossRef]
50. Dong, Z.; Liu, Y.; Wen, W.; Ge, J.; Liang, J. Effect of Hatch Spacing on Melt Pool and As-built Quality During Selective Laser Melting of Stainless Steel: Modeling and Experimental Approaches. *Materials* **2019**, *12*, 50. [CrossRef]
51. Caiazzo, F.; Alfieri, V.; Casalino, G. On the Relevance of Volumetric Energy Density in the Investigation of Inconel 718 Laser Powder Bed Fusion. *Materials* **2020**, *13*, 538. [CrossRef]
52. Li, Y.; Založnik, M.; Zollinger, J.; Dembinski, L.; Mathieu, M. Effects of the powder, laser parameters and surface conditions on the molten pool formation in the selective laser melting of IN718. *J. Mater. Process. Technol.* **2021**, *289*, 116930. [CrossRef]
53. Chen, Q.; Zhao, Y.; Strayer, S.; Zhao, Y.; Aoyagi, K.; Koizumi, Y.; Chiba, A.; Xiong, W.; To, A.C. Elucidating the effect of preheating temperature on melt pool morphology variation in Inconel 718 laser powder bed fusion via simulation and experiment. *Addit. Manuf.* **2021**, *37*, 101642. [CrossRef]
54. Baldi, N.; Giorgetti, A.; Palladino, M.; Arcidiacono, G.; Citti, P. Study on the Effect of Interlayer Cooling Time on the Microstructure of IN718 processed by Laser Powder Bed Fusion. *Addit. Manuf. forthcoming*.
55. Yadroitsev, I.; Krakhmalev, P.; Yadroitsava, I. Hierarchical design principles of selective laser melting for high quality metallic objects. *Addit. Manuf.* **2015**, *7*, 45–56. [CrossRef]
56. Tran, H.C.; Lo, Y.L. Systematic approach for determining optimal processing parameters to produce parts with high density in selective laser melting process. *Int. J. Adv. Manuf. Technol.* **2019**, *105*, 4443–4460. [CrossRef]